

See discussions, stats, and author profiles for this publication at: <https://www.researchgate.net/publication/312178176>

# Automatic Nuclear Segmentation Using Multiscale Radial Line Scanning With Dynamic Programming

Article in IEEE Transactions on Biomedical Engineering · January 2017

DOI: 10.1109/TBME.2017.2649485

CITATIONS

4

READS

196

5 authors, including:



**Hongming Xu**  
Cleveland Clinic

21 PUBLICATIONS 113 CITATIONS

[SEE PROFILE](#)



**Cheng Lu**  
Case Western Reserve University

41 PUBLICATIONS 316 CITATIONS

[SEE PROFILE](#)



**Richard Berendt**  
University of Alberta

29 PUBLICATIONS 469 CITATIONS

[SEE PROFILE](#)



**Naresh Jha**  
Cross Cancer Institute

68 PUBLICATIONS 1,746 CITATIONS

[SEE PROFILE](#)

Some of the authors of this publication are also working on these related projects:



Histomorphometrics and its application in Cancer prognosis [View project](#)



biopsy image analysis [View project](#)

# Automatic Nuclear Segmentation Using Multi-scale Radial Line Scanning with Dynamic Programming

Hongming Xu, Cheng Lu, Richard Berendt, Naresh Jha, and Mrinal Mandal, *Senior Member, IEEE*

**Abstract**—In the diagnosis of various cancers by analyzing histological images, automatic nuclear segmentation is an important step. However, nuclear segmentation is a difficult problem because of overlapping nuclei, inhomogeneous staining, and presence of noisy pixels and other tissue components. In this paper, we present an automatic technique for nuclear segmentation in skin histological images. The proposed technique first applies a bank of generalized Laplacian of Gaussian (gLoG) kernels to detect nuclear seeds. Based on the detected nuclear seeds, a multi-scale radial line scanning (mRLS) method combined with dynamic programming (DP) is applied to extract a set of candidate nuclear boundaries. The gradient, intensity and shape information are then integrated to determine the optimal boundary for each nucleus in the image. Nuclear overlap limitation is finally imposed based on a Dice coefficient measure such that the obtained nuclear contours do not severely intersect with each other. Experiments have been thoroughly performed on two datasets with H&E and Ki-67 stained images, which shows that the proposed technique is superior to conventional schemes of nuclear segmentation.

**Index Terms**—Nuclear segmentation, seeds detection, dynamic programming, histological images, H&E staining.

## I. INTRODUCTION

EVALUATION of cell nuclei plays an important role in the histopathological examination and analysis of digitized slides. The parameters like cell size, shape, contours and presence or absence of nucleoli are generally used by pathologists for various cancer diagnosis. The abnormal cell distributions and morphological changes often indicate the malignancy of the lesion [1], [2]. However, manual counting and segmentation of cell nuclei is a very tedious work, and also prone to inter- or intra-observer variability due to poor contrast and clumping of nuclei. To reduce the workload and obtain more objective results, many efforts have been devoted to develop automatic nuclear segmentation techniques.

Threshold-based techniques have been widely used for nuclear segmentation in histological images. These works are related to segmentation of cell nuclei in the digitized neuroblastoma slides [3], breast histopathological images [4] and skin histopathological images [5]. A major limitation of

these threshold-based techniques is the under-segmentation of clumped cell nuclei. In order to address this issue, a number of techniques for cellular or nuclear clumps segmentation have been reported. These techniques mainly includes two categories: concavity analysis based techniques [6]–[12], and “seed” (or “marker”) based techniques [13]–[18].

For concavity analysis based techniques, the first step is to identify valid concave points for splitting. Several techniques exist for identifying concave points on the contour. For example, the concave points have been detected based on computing the cross product of vectors defined by three consecutive points [6], or minimizing a cost function to find the bottleneck positions on the contour [7]. With detected concave points, the next step is to connect them and split cellular or nuclear clumps into isolated ones. This step can be achieved iteratively by connecting the shortest path between concave points until all split regions are considered to be isolated [11]. Although concavity analysis based techniques have been reported to provide a good performance, the performance is overly sensitive to image binarizations, and the predefined thresholds (usually several thresholds) that are used for finding valid concave points [7], [10].

For “seed” (or “marker”) based techniques, the first step is to identify “seeds” for nuclear regions. These detected “seeds” are usually close to nuclear centers, and used as the starting points for active contours or watershed segmentation. The segmentation performance depends critically on the accuracy and reliability of initial seed points. Because of the advantages of simplicity, speed and absence of adjustable parameters, several marked watershed algorithms have been developed for cellular or nuclear segmentation. For example, the markers of watershed algorithm are detected by condition erosion [15], H-minima transform [16], [17], improved voting algorithm [14] and radial symmetry transform [18]. These watershed based segmentations are heavily relied on the accuracy of image binarizations as the topographic surfaces for segmentation are built from distance maps of binary images. In order to get more accurate segmentations, Al-Kofahi et al. [19] proposed a multi-scale Laplacian of Gaussian (mLoG) filter based technique, which detects nuclei by mLoG filters and segments nuclei based on size-constrained clustering with further refinement by a graph cuts based algorithm. Qi et al. [13] proposed to detect cell seeds in breast histopathological images by a single pass voting algorithm and delineate cell contours by a repulsive level set model [20]. Xing et al. [21] proposed a cell detection and segmentation technique for evaluating Ki-67 proliferation index in gauge neuroendocrine tumor images. This technique detects cell seeds by a hierarchical voting

H. Xu and M. Mandal are with the Department of Electrical and Computer Engineering, University of Alberta, Edmonton, AB, T6G 1H9 Canada (e-mail: mxu@ualberta.ca, mmandal@ualberta.ca).

C. Lu is with the College of Computer Science, Shaanxi Normal University, Xi'an, Shaanxi Province, 710119 China, and the Department of Biomedical Engineering, Case Western Reserve University, Cleveland OH, 44106 USA (e-mail: chengluc@snu.edu.cn).

R. Berendt and N. Jha are with the Department of Oncology, Cross Cancer Institute, University of Alberta, Edmonton, AB, T6G 1Z2 Canada (e-mail: richard.berendt@albertainhealthservices.ca, naresh.jha@albertainhealthservices.ca).

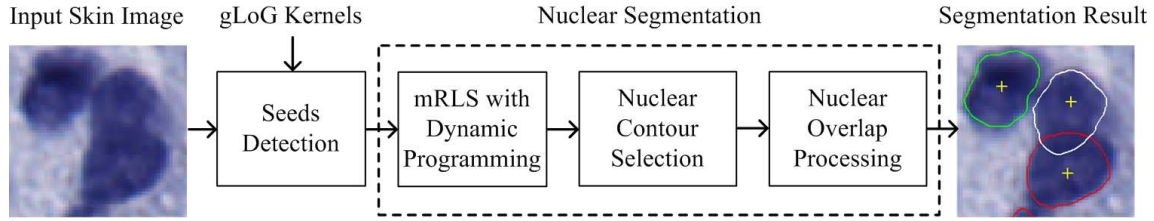


Fig. 1. Schematic of the proposed technique.

method, and delineates cell boundaries by a repulsive active contour model. Zhang et al. [22] further combined the cellular segmentation technique in [21] with hashing based retrieval approach for differentiation of two types of lung cancers (i.e., adenocarcinoma and squamous carcinoma). The active contours based techniques tend to provide more accurate segmentations, but they (e.g., in [13], [21]) cannot delineate occluded nuclear boundaries for overlapping nuclei.

Recently a few techniques based on active shape models and deep learning (DL) have been proposed for nuclear segmentation. Plissiti et al. [23] proposed a technique that segments overlapping cell nuclei by driving the deformable model based on physical principals, but this technique only works automatically for the image with a known number of cell nuclei. Lu et al. [24] proposed a technique to perform cervical cell segmentation by joint optimization of multiple level set functions. This technique has a high computational complexity and its performance is critically relied on initial segmentations for level set functions. Janowczyk et al. [25] proposed a resolution adaptive deep hierarchical (RADHical) learning scheme for nuclear segmentation in histological images. The RADHical employs the AlexNet network [26] in a multi-resolution framework, which classifies most of image pixels at low resolutions and only processes uncertain regions at high resolutions. The RADHical provides a similar performance with the naive DL model [27] that processes the high-resolution images directly, but it achieves about 6 times speed improvement. Although the DL methods are very powerful to learn image features, they are generally quite time-consuming to train and apply.

Besides the above mentioned methods, graph theories are also used for medical tissue segmentations. Li et al. [28] proposed a segmentation method for volumetric images (e.g., pulmonary CT images) by computing a minimum  $s$ - $t$  cut in a derived arc-weighted directed graph. Zhang et al. [29] proposed a graph search based method for intestinal gland segmentation in histological images. The method uses a graph search algorithm to generate the gland boundary probability map. The watershed algorithm is then applied on the boundary probability map to perform segmentations. The graph search methods have the potential to be used for nuclear segmentations, but it is difficult to determine an optimal graph search radius due to nuclear size variations and existence of clustered nuclei.

In this paper, we propose a “seed” based technique for nuclear segmentation in histological images, which can resolve nuclear overlap and obtain occluded nuclear boundaries

in clumped nuclei. The proposed technique detects nuclear seeds by using a set of multi-scale gLoG kernels. For each nucleus, several boundaries are delineated by a mRLS method combined with DP. The optimal nuclear boundary is then determined by making use of gradient, intensity and nuclear shape information. Severely overlapped nuclei are finally resolved based on the Dice coefficient measure. The organization of this paper is as follows. Section II describes the proposed technique, followed by the performance evaluations in Section III. The conclusion is presented in Section IV.

## II. PROPOSED TECHNIQUE

The schematic of the proposed technique for nuclear segmentation is shown in Fig. 1. It is observed that there are two main modules. In the first module, nuclear seeds are detected using a bank of gLoG kernels with different scales and orientations. In the second module, nuclear boundaries are delineated by using a multi-scale radial line scanning (mRLS) based method. This method consists of three sub-modules. The first module estimates candidate nuclear contours using mRLS with DP based on gradient information. The second module selects the optimal nuclear contours by integrating nuclear intensity and shape prior with gradient information. The third module resolves overlapped nuclei based on a predefined area-overlapping allowance. In the following, we explain the two modules with an emphasis on nuclear segmentation module.

### A. Seeds Detection

Because cell nuclei in digitized histological images typically have circular or elliptical shapes, we apply a gLoG kernels based technique [30] to detect nuclear seeds. This technique first generates a bank of gLoG kernels with different scales and orientations. The gLoG kernel  $\nabla^2 G(x, y)$  is defined as:

$$\nabla^2 G(x, y) = \frac{\partial G(x, y; \sigma_x, \sigma_y, \theta)}{\partial x^2} + \frac{\partial G(x, y; \sigma_x, \sigma_y, \theta)}{\partial y^2} \quad (1)$$

where  $G(x, y; \sigma_x, \sigma_y, \theta)$  is a generalized Gaussian kernel with scales  $(\sigma_x, \sigma_y)$  and orientation  $\theta$  [30]. After generating multi-scale gLoG kernels, the same directional kernels are aggregated together and convolved with the image  $I(x, y)$  (the red channel of original color image) to generate response maps. The points of local maxima are then searched from multiple response maps and clustered into different groups using mean-shift algorithm [31]. Finally, the geometrical means of local maxima points in different groups are computed and considered as nuclear seeds. Fig. 2 shows examples of gLoG kernels with different scales and orientations. Fig. 3(a) shows

two skin histological images where nuclei are observed as blue blobs. Fig. 3(b) shows seeds detection result using gLoG kernels shown in Fig. 2 (e.g., 95 gLoG kernels), where the detected seeds are indicated by (yellow) crosses. Note that in Fig. 3 the skin image in the first row is stained with Ki-67, and the image in the second row is stained with H&E. As observed in Fig. 3, nuclei have been correctly detected by the gLoG kernels based method [30].

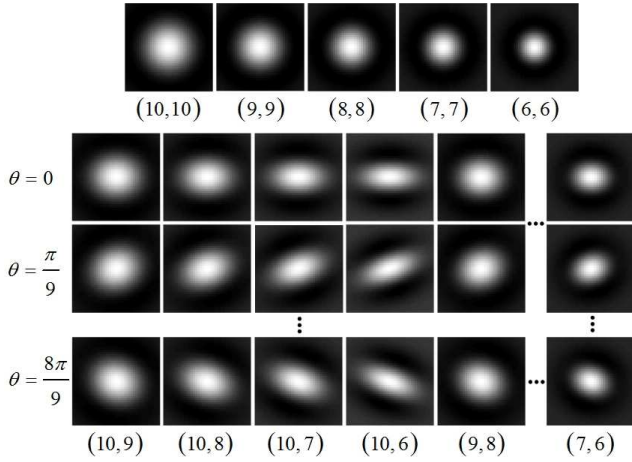


Fig. 2. gLoG kernels. Note that parameters  $(\cdot, \cdot)$  below a kernel correspond to  $(\sigma_x, \sigma_y)$ .

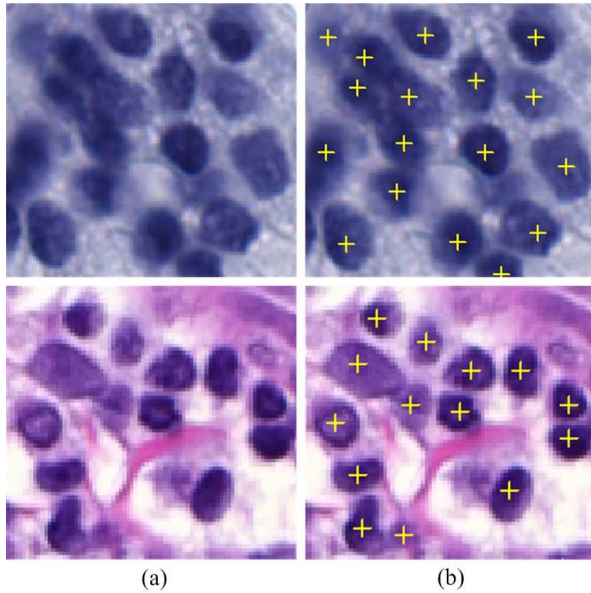


Fig. 3. Nuclear detections. (a) Skin images. (c) Nuclear detection results. Symbols + in (b) indicate detected nuclear seeds. The image in the first row is stained with Ki-67, and the image in the second row is stained with H&E.

### B. Nuclear Segmentation

After detecting nuclear seeds, the next step is to delineate nuclear boundaries. In order to capture nuclear boundaries, we propose a mRLS based technique in this module. In the following, we explain the mRLS based technique in three sub-modules: mRLS with DP, nuclear contour selection and

nuclear overlap processing. Details of these three modules are as follows:

1) *mRLS with DP*: The radial line scanning (RLS) method has been successfully used to detect melanocytes in our previous work [32]. To utilize the RLS method, the detected seeds are considered as nuclear centers. A set of radial lines emerging from the nuclear center are then computed. These radial lines have radial orientations as follows:

$$\theta_i = \frac{2\pi}{N} (i - 1), \quad i = 1 \dots N \quad (2)$$

where  $N$  indicates the number of radial lines. For each radial line, we denote the minimum scanning radius as  $R_S$  and maximum scanning radius as  $R_E$ . Fig. 4(a) illustrates an example of scanning radii for one radial line, where  $\theta_1 = 0$ . Fig. 4(b) shows a real example with 30 radial lines (i.e.,  $N = 30$ ) emerging from the detected nuclear seed. The (yellow) contour in Fig. 4(b) is the reference nuclear boundary. As observed in Fig. 4(b), each radial line intersects the nuclear boundary at only one point. Let us assume there are  $M$  discrete points on each radial line between  $R_S$  (green circle) and  $R_E$  (blue circle). Hence, we have  $M^N$  different possible closed contours, where a contour uses only one point in each of  $N$  lines. The nuclear boundary shown in Fig. 4(b) is one of these possible configurations.

In order to automatically delineate a nuclear boundary (like that shown in Fig. 4(b)) from  $M^N$  different configurations, image gradient is utilized. Since the original image  $I(x, y)$  usually includes noisy pixels, a smooth image  $I_s(x, y)$  is first obtained by convolving the image with a Gaussian kernel as follows:

$$I_s(x, y) = G(x, y; \sigma) * I(x, y) \quad (3)$$

where  $G(x, y; \sigma) = \sigma^{-1/2} e^{-(x^2+y^2)/4\sigma}$ . The gradient magnitude map  $\mathcal{G}_m(x, y)$  and gradient direction map  $\mathcal{G}_d(x, y)$  are then generated using following equations: 计算梯度图 (大小及方向)

$$\mathcal{G}_m(x, y) = \sqrt{\left(\frac{\partial I_s(x, y)}{\partial x}\right)^2 + \left(\frac{\partial I_s(x, y)}{\partial y}\right)^2} \quad (4)$$

$$\mathcal{G}_d(x, y) = \arctan\left(\frac{\partial I_s(x, y)}{\partial y} / \frac{\partial I_s(x, y)}{\partial x}\right) \quad (5)$$

Fig. 4(c) shows a close-up view of nucleus overlapped with the gradient map, where gradients are indicated by arrows. As seen in Fig. 4(c), the reference nuclear boundary consists of high gradient points. In addition, if assuming that the directions of radial lines are outward (i.e., pointing from the nuclear center to the boundary), nuclear boundary points have gradient directions similar to that of corresponding radial lines. Based on these observations, we append a cost value for each point of the  $M$  discrete points on the  $i$ th radial line. The appended cost value  $C(p_i)$  is computed as:

$$\text{maximize } C(p_i) = \alpha \cos(|\theta_i - \mathcal{G}_d(p_i)|) + \beta \mathcal{G}'_m(p_i) \quad (6)$$

where  $\alpha$  and  $\beta$  are weights of gradient directions and magnitudes, respectively.  $\mathcal{G}'_m(p_i)$  is the normalized  $\mathcal{G}_m(p_i)$ , which is calculated as follows:

$$\mathcal{G}'_m(p_i) = \frac{\mathcal{G}_m(p_i)}{\max \mathcal{G}_m(p_i)}, \quad 1 \leq i \leq N \quad (7)$$



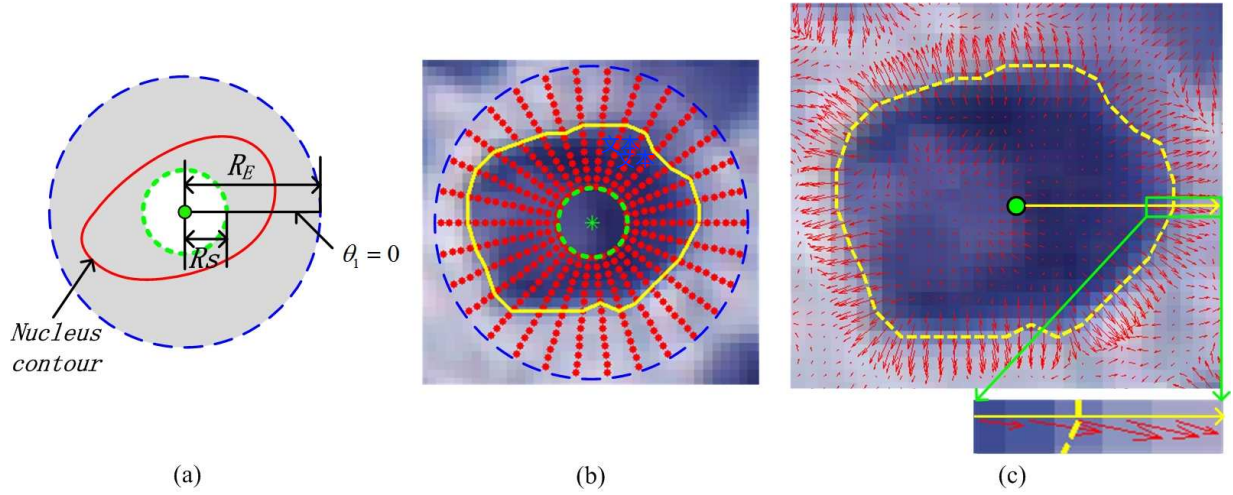


Fig. 4. Illustration of radial line scanning. (a) Scanning radii of one radial line. (b) 30 radial lines emerging from a detected nuclear seed. (c) Gradient map overlapped on a nuclear image. Note that in (b)(c) nuclear boundaries are indicted by yellow contours.

Note that in (6) the gradient direction is incorporated into the cost value  $C(p_i)$ , which can suppress undesirable influence of high gradient points from other neighboring nuclear boundaries. This is because orientations of radial lines for one nucleus, in an ideal case, are opposite to gradient directions of other neighboring nuclear boundaries.

After appending a cost value to each point of radial lines, it might appear that points of nuclear boundaries can be selected by maximizing the cost value  $C(p_i)$  in each radial line. However, such simple selection of boundary points is difficult to obtain a smooth nuclear contour, as the determined boundary points are prone to be disturbed by isolated high gradient noisy pixels. In order to obtain accurate and smooth nuclear contours, we consider all radial lines together and define the following cost function (corresponding to a nuclear *gradient*):

$$E_{\text{gradient}}(p_1, p_2, \dots, p_N) = E_1(p_1, p_2) + E_2(p_2, p_3) + \dots + E_{N-1}(p_{N-1}, p_N) + E_N(p_N, p_1) \quad (8)$$

where each additive cost value  $E_i$  is calculated as:

$$E_i(p_i, p_{i+1}) = \begin{cases} \kappa - C(p_i) & \text{if } D(p_i, p_{i+1}) \leq \delta \\ \infty & \text{otherwise} \end{cases} \quad (9)$$

where  $\kappa = \max C(p_i)$ ,  $1 \leq i \leq N$ .  $D(p_i, p_{i+1})$  is the Euclidean distance between points  $p_i$  and  $p_{i+1}$ , and  $\delta$  is a predefined distance value (e.g.,  $\delta = 1$ ). Note that the cost function in (8) has a typical overlapping and additive form that can be efficiently optimized by DP in  $O(NM^2)$  computations [33]. The cost component (9) implies that if the Euclidean distance  $D$  between two consecutive points on the contour are within a predefined distance  $\delta$ , the cost value  $E_i$  equals to  $\kappa - C(p_i)$ . Otherwise the cost value is assigned to be positive infinity. With (9) as the individual cost component, the net effect of minimizing (8) would be to obtain a contour consisting of points with high gradient magnitudes and gradient directions similar to orientations of corresponding radial lines. Besides, any two consecutive points on the contour have the Euclidean distance smaller than  $\delta$ .

Although the RLS technique with DP can generally provide smooth and accurate nuclear contours, the technique is relatively sensitive to the parameter  $R_E$  (the maximal scanning radius). This is because nuclear size and shape in histological images (even for the same type of images) usually vary from each other, and there exist touching and overlapping nuclei in 2-D images. When a small  $R_E$  value is applied, the large nuclei in the image may be truncated (see Figs. 6(c)(d) with arrows). However, when a large  $R_E$  value is applied, it not only increases the computational complexity but also may under-split clustered nuclei (see Figs. 6(e)(f) with arrows). Therefore, it is difficult to obtain accurate nuclear contours for all nuclei in a large image by using a fixed  $R_E$  value.

In order to overcome this limitation, we propose to use a set of  $R_E$  values (i.e.,  $R_E^{\min} \leq R_E \leq R_E^{\max}$ ) rather than a fixed value to adapt nuclear size variations. The parameters  $R_E^{\min}$  and  $R_E^{\max}$  can be estimated based on nuclear radii in the image. Using a set of  $R_E$  values (or mRLS with DP), each nucleus has several obtained contours. For example, Fig. 5(a) shows a skin image with three cell nuclei. Figs. 5(b)-(f) show the nuclear contours obtained by the mRLS technique with DP, where  $R_S = 3$  and  $R_E = \{14, 15, 16, 17, 18\}$ , respectively. As observed in Figs. 5(b)-(f), with different  $R_E$  values, each nucleus has several different obtained contours. Since there are several candidate contours for each nucleus, the optimal contour is to be determined in the next module.

2) *Nuclear Contour Selection*: Several boundary contours are obtained for every nucleus by using the mRLS with DP. In this module, we select the optimal contour for each nucleus. In order to select the optimal contour, we integrate nuclear intensity variance and shape prior with the gradient information (obtained by (8)). Based on the observation that nuclear blobs in our dataset have relatively homogeneous intensities, the cost component corresponding to the *intensity variance* is defined as follows:

$$E_{\text{intensity}} = \iint_{(x,y) \in \Omega_N} |I(x,y) - c|^2 dx dy \quad (10)$$

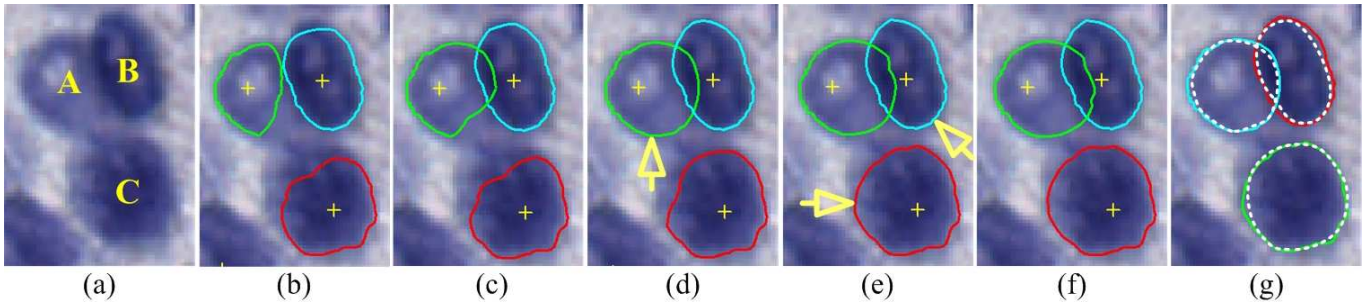


Fig. 5. Nuclear segmentations. (a) A skin image with three cell nuclei (40X magnification). (b)  $R_E = 14$ . (c)  $R_E = 15$ . (d)  $R_E = 16$ . (e)  $R_E = 17$ . (f)  $R_E = 18$ . (g) Automatic segmentations compared with manual segmentations (shown as dotted contours). Note that parameter settings for mRLS with DP are:  $N = 100$ ,  $R_S = 3$ ,  $\alpha = 1.0$ , and  $\beta = 0.5$ . In (b)-(f) symbols + are the detected nuclear seeds. In (d)(e) arrows indicate optimal nuclear contours which are selected as the final nuclear contours shown in (g).

TABLE I  
COST VALUES  $E_{total}$  FOR NUCLEI SHOWN IN FIG. 5.

Nuclei	$E_{total}$				
	$R_E=14$	$R_E=15$	$R_E=16$	$R_E=17$	$R_E=18$
A	1.66	1.57	<b>1.47</b>	1.52	1.50
B	1.74	1.59	1.49	<b>1.48</b>	1.48
C	1.62	1.64	1.60	<b>1.52</b>	1.54

where  $\Omega_N$  denotes a segmented nucleus region, and  $c$  is the mean intensity in the region  $\Omega_N$ . Note that a smaller  $E_{intensity}$  value indicates a more homogeneous nucleus region.

The nuclei typically have circular or elliptical shapes, and hence the shape prior is incorporated for nuclear contour selection. Given a nuclear region  $\Omega_N$ , an elliptical region  $\Omega_E$  that has the same second moments as  $\Omega_N$  is obtained by the ellipse-fitting algorithm [34]. Let  $\mathcal{A}_n$  and  $\mathcal{A}_e$  be the sets of pixels in  $\Omega_N$  and  $\Omega_E$ , respectively. The cost component  $E_{shape}$  corresponding to a nuclear shape is computed as follows:

$$E_{shape} = 1 - \frac{|\mathcal{A}_n \cap \mathcal{A}_e|}{|\mathcal{A}_e|} \quad (11)$$

where  $|\cdot|$  is the cardinality of pixels set and  $\cap$  is intersection operation.  $E_{shape}$  has a dynamic range of  $[0, 1)$ , and a smaller value of the  $E_{shape}$  represents a closer match to an elliptical shape.

Let  $\mathbf{E}_{gradient}$  be a vector of  $E_{gradient}$  obtained by (8) with different  $R_E$  values. Similarly, let  $\mathbf{E}_{intensity}$  and  $\mathbf{E}_{shape}$  be the vectors of  $E_{intensity}$  (10) and  $E_{shape}$  (11), respectively. We integrate gradient, intensity and shape information together and define the following energy cost function:

$$\mathbf{E}_{total} = \lambda_1 \frac{\mathbf{E}_{gradient}}{\|\mathbf{E}_{gradient}\|} + \lambda_2 \frac{\mathbf{E}_{intensity}}{\|\mathbf{E}_{intensity}\|} + \lambda_3 \frac{\mathbf{E}_{shape}}{\|\mathbf{E}_{shape}\|} \quad (12)$$

where  $\lambda_1$ ,  $\lambda_2$  and  $\lambda_3$  are weights of each term, and  $\|\cdot\|$  is the Euclidean norm. Note that  $\mathbf{E}_{total}$  is a vector of overall cost function for different  $R_E$  values.  $\mathbf{E}_{gradient}$  assures that nuclear boundaries are located on high gradient points.  $\mathbf{E}_{intensity}$  assures that the segmented nuclear region is homogenous.  $\mathbf{E}_{shape}$  assures that the segmented nuclear region has an elliptical shape. By selecting the minimal cost value in (12), it

is expected to obtain a nuclear boundary lying on high gradient points and surrounding a region with an elliptical shape and homogeneous intensities. The parameters  $\lambda_1$ ,  $\lambda_2$  and  $\lambda_3$  can be adaptively adjusted according to different applications. For instance, a smaller value  $\lambda_2$  can be utilized when nuclear regions in testing images are not homogeneous. In this work, we have empirically set them as:  $\lambda_1 = 1$ ,  $\lambda_2 = 1$  and  $\lambda_3 = 1$ . Table I lists the costs  $E_{total}$  for nuclei A, B and C shown in Fig. 5(a), where  $R_S = 3$ ,  $14 \leq R_E \leq 18$ . It is observed in Table I that the cost  $E_{total}$  for the nucleus A is the smallest when  $R_E = 16$ . In other words, the optimal nuclear contour, as indicated by the arrow in Fig. 5(d), is obtained when  $R_E = 16$ . For nuclei B and C, the optimal nuclear contours, as indicated by arrows in Fig. 5(e), are obtained when  $R_E = 17$ . Fig. 5(g) compares the finally obtained nuclear contours (i.e., the optimal contours shown in Figs. 5(d)(e)) with manually labeled nuclear boundaries (shown as dotted contours). As seen in Fig. 5(g), the automatically obtained nuclear contours by the mRLS based technique have a good matching with manually labeled nuclear contours.

To further illustrate the advantages of the mRLS based technique, two examples of elliptical blobs segmentation are shown in Fig. 6. The top row of Fig. 6 shows a synthetic image with three elliptical blobs and Gaussian white noise (with 0.1 variance), and the bottom row shows a H&E stained skin image. Figs. 6(c)(d) show blob segmentations with  $R_S = 3$  and  $R_E = 7$ , where inaccurately-segmented blobs (indicated by hollow arrows) have been observed in both synthetic and real images due to a small  $R_E$  value used. Figs. 6(e)(f) show blob segmentations with  $R_S = 3$  and  $R_E = 11$ . In Figs. 6(e)(f) although the inaccurately-segmented blobs in (c)(d) have been correctly segmented, inaccurate segmentations (indicated by solid arrows) have been observed for some other blobs because of a large  $R_E$  value used. Figs. 6(g)(h) show blob segmentations by the mRLS based technique, where  $R_S = 3$  and  $7 \leq R_E \leq 11$ . It is observed that segmentation results in Figs. 6(g)(h) are more accurate than those in Figs. 6(c)(d)(e)(f), respectively.

3) *Nuclear Overlap Processing*: In previous steps, we presented a procedure to delineate each nucleus individually. The obtained nuclear contours may intersect with each other (see Fig. 5(g)), as cell nuclei usually overlap or touch together in 2-D images. Note that although excessive or sometimes



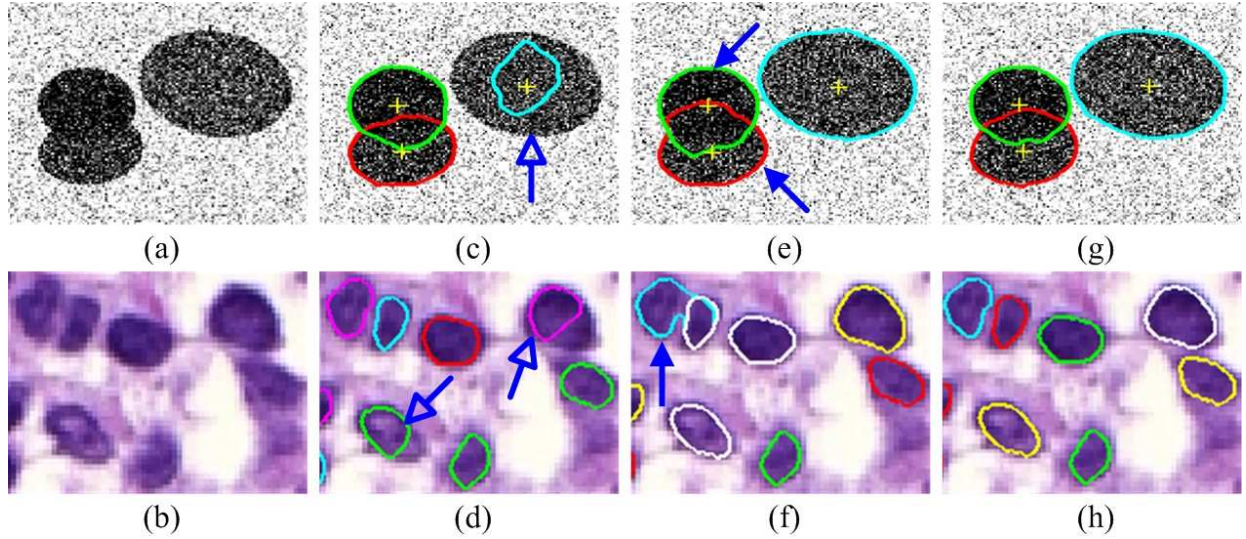


Fig. 6. Blob segmentations. (a) A synthetic image with three blobs. (b) An H&E stained skin image (25X magnification). (c)&(d)  $R_S = 3$ ,  $R_E = 7$ . (e)&(f)  $R_S = 3$ ,  $R_E = 11$ . (g)&(h)  $R_S = 3$  and  $7 \leq R_E \leq 11$ . In (c)(d)(e)(f) arrows indicate inaccurate segmentations.

complete overlap may also be occurred in real cases, manual evaluations usually consider excessively overlapped nuclei as single nucleus. In this module, we impose an overlap allowance limitation such that the segmented nuclear regions do not severely overlap with each other. The overlap limitation is imposed based on the Dice coefficient. Specially, for each group of overlapped nuclei, the following steps are iteratively applied until the stop criteria:

Step 1: Let  $s$  denote the number of individual candidate nucleus in the overlapped nuclei region. The Dice coefficient for two cell nuclei  $i$  and  $j$  is computed as follows:

$$D(\mathcal{A}_i, \mathcal{A}_j) = \frac{2 \times |\mathcal{A}_i \cap \mathcal{A}_j|}{|\mathcal{A}_i| + |\mathcal{A}_j|} \quad (13)$$

where  $\mathcal{A}_i$  and  $\mathcal{A}_j$  denote the set of pixels in the  $i$ th and  $j$ th nuclear regions,  $1 \leq \{i, j\} \leq s$ ,  $i \neq j$ . The Dice coefficient  $D(\mathcal{A}_i, \mathcal{A}_j)$  is a distance measure to evaluate the similarity of two sets [18]. The measure has a maximum value of 1 when two nuclear regions are completely overlapped with each other and a minimum value of 0 when two nuclear regions do not intersect.

Step 2: In this step, we first compute the largest Dice coefficient among  $s(s-1)/2$  pairs of overlapped nuclei. Let us assume that the  $m$ th and  $n$ th nuclei have the largest Dice coefficient. If  $D(\mathcal{A}_m, \mathcal{A}_n)$  satisfies the following stop condition:

$$D(\mathcal{A}_m, \mathcal{A}_n) < \tau \quad (14)$$

where  $\tau$  is a predefined overlap allowance (e.g.,  $\tau = 0.6$ ), then the overlap processing stops. Otherwise, if  $E_{total}(\mathcal{A}_m) < E_{total}(\mathcal{A}_n)$ , the  $m$ th nucleus is kept and the  $n$ th nucleus is discarded, and vice versa. If this happens, the  $s$  value is reduced by 1 and the algorithm goes to the Step 3. Note that the cost values  $E_{total}(\mathcal{A}_m)$  and  $E_{total}(\mathcal{A}_n)$  are obtained by minimizing (12).

Step 3: If (14) is not satisfied and  $s > 1$ , we repeat Step 1 and Step 2. Otherwise, the algorithm stops.

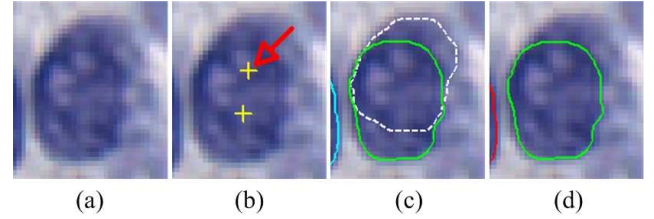


Fig. 7. Nuclear overlap processing. (a) A nucleus. (b) An nucleus with two seeds (where the false seed is indicated by the red arrow). (c) Nuclear boundaries obtained by the mRLS based technique. (d) Final nuclear boundary after overlap processing.

By utilizing the above three steps, we try to add an overlap allowance for clustered nuclei such that the segmented nuclei are not severely overlapped with each other. Fig. 7(a) shows a cell nucleus, and Fig. 7(b) shows two detected nuclear seeds. Fig. 7(c) shows the obtained nuclear contours based on the two detected seeds, where segmented nuclear regions severely overlap with each other. Figs. 7(d) shows the finally obtained nuclear contour after overlap processing, where the dashed (white) nuclear contour in Fig. 7(c) has been discarded.

### III. PERFORMANCE EVALUATIONS

In this section, we evaluate the performance of the proposed technique. First we illustrate the testing datasets used in this work. We then present the quantitative and qualitative evaluations of the proposed technique and several existing techniques for nuclear segmentation.

#### A. Datasets Description

This study was based on two datasets of skin histopathological images which were collected from the Cross Cancer Institute, University of Alberta. The first dataset (Dataset-I) consists of 40 Ki-67 stained skin images which were cropped from four digital biopsy slides. The biopsy slides were digitized under 40X magnification on Aperio Scanscope

CS scanning system. The images have a pixel resolution of  $0.248\mu\text{m}/\text{pixel}$ , and include 1446 manually identified cell nuclei in total. The second dataset (Dataset-II) consists of 28 H&E stained skin images which were cropped from five biopsy slides. The biopsy slides were digitized under 25X magnification on Carl Zeiss MIRAX MIDI scanning system. These images have a pixel resolution of  $0.372\mu\text{m}/\text{pixel}$ , and include 714 manually identified cell nuclei in total. Note that all nuclear centroids in Datasets-I and II were first manually labeled by an imaging expert with over 3 years of experience on skin pathology. The results were then examined and fine-tuned by an experienced pathologist, and finally used as the ground truth seeds.

### B. Quantitative Evaluations

To illustrate the efficacy of nuclear segmentation, the performance of the proposed technique is compared with several existing techniques including local optimal thresholding (LOT) [5], marker optimization with watershed algorithm (MOW) [17], improved voting with watershed algorithm (IVW) [14], repulsive active contours model (RACM) [21], deep learning method (DLM) [35] and graph search based method (GSM) [29]. The LOT technique is chosen as the baseline thresholding method, and it segments cell nuclei based on two prior knowledge: nuclear size and shape. There are two key parameters namely predefined nuclear area range  $[A_{\min}, A_{\max}]$  that should be adaptively selected when using the LOT technique. We have experimentally set them as  $[400, 900]$  and  $[100, 400]$  for our Datasets-I, II, respectively. The MOW technique segments cell nuclei based on H-minima transform and watershed algorithm. There is only one key parameter namely angular margin  $\omega$  that is used to avoid over-segmentation by the MOW technique. As verified in [17], the MOW technique is not very sensitive to the parameter  $\omega$ , and hence it is set as  $\pi/12$  (the same as that in [17]) for comparisons. Both the IVW and RACM techniques detect nuclear seeds by a voting procedure, where the voting radial range  $[r_{\min}, r_{\max}]$  and the bandwidth  $b_w$  of mean-shift clustering are the key parameters determining nuclear detection performance. The voting radial range  $[r_{\min}, r_{\max}]$  are estimated based on nuclear radii, which are set as  $[5, 16]$  and  $[2, 9]$  for our Datasets I, II, respectively. The bandwidth  $b_w$  is adaptively set as  $(r_{\min} + r_{\max})/2$ , as was done in [14]. After detecting nuclear seeds, the RACM technique delineates nuclear boundaries by the active contours model with a repulsive term to prevent evolving contours from crossing and merging with one another. There are a few weight parameters ( $\alpha$ ,  $\beta$ ,  $\gamma$ ,  $\lambda$  and  $\eta$ ), which controls the elasticity, rigidity, pressure force, image force and repulsive force of the active contour model, respectively. We have experimentally set these parameters as:  $\alpha = 0.05$ ,  $\beta = 0$ ,  $\gamma = 0.25$ ,  $\lambda = 2$  and  $\eta = 1$  for our two datasets. For the DLM, we implemented the VGG style CNN [35] with Batch Normalization technique [36]. Specifically, a 9 layers DL architecture which consists of 1 input layer, 6 convolution layers, 1 fully connected layer and 1 output layer is constructed. The input layer accepts an image patch of  $64 \times 64$  pixels, and the output layer is a soft-max function which outputs the class

probability of being nucleus or non-nucleus. During training, we randomly select 20 images from each of our Datasets-I and II as training samples, and the DL architecture is trained following the procedure proposed by [27]. During testing, a threshold of 0.3 is experimentally selected to binarize the probability map output by the DLM. The GSM is originally proposed for intestinal gland segmentation in H&E stained biopsy images. We adaptively modified it to perform nuclear segmentation for comparison with the proposed technique. In our implementation, we utilize the gradient magnitude as graph node weights instead of using image intensity information like [29], as nuclear boundaries tend to be located on high gradient points (rather than low intensity points). The graph search radii are set as 18 and 11 pixels in our Datasets-I and II, respectively. After obtaining boundary probability map by graph search, watershed segmentation is performed with false nuclear regions removed based on area and color analysis.

Automatic segmentation results by different methods have been manually inspected by an interactive software (based on Matlab). Let  $N_{CS}$ ,  $N_{OS}$ ,  $N_{US}$  and  $N_{ER}$  represent the numbers of correct-segmentation (CS), over-segmentation (OS), under-segmentation (US) and encroachment errors (ER). Note that OS refers to excessive splitting (i.e., one nuclear region is split into two subregions as shown in Fig. 8(b)). US refers to the failure to split nuclear regions into the correct number of nuclei (see Fig. 8(c)). ER refers to the case that automatically obtained nuclear boundaries are visually not accurate (see Fig. 8(d)). The performance of nuclear segmentations has been evaluated by several widely-used evaluation metrics [11], [19]: CS, OS, UR and ER rates, which are defined as follows:

$$CS = \frac{N_{CS}}{N_{GT}} \times 100\%, \quad OS = \frac{N_{OS}}{N_{GT}} \times 100\% \quad (15)$$

$$US = \frac{N_{US}}{N_{GT}} \times 100\%, \quad ER = \frac{N_{ER}}{N_{GT}} \times 100\% \quad (16)$$

where  $N_{GT}$  represents the number of manually identified (ground truth) nuclei.

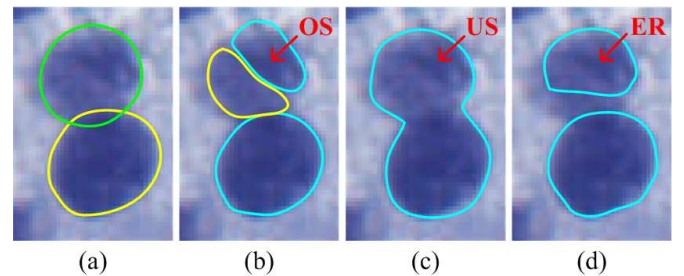


Fig. 8. Illustration of over-segmentation, under-segmentation and encroachment errors. (a) Two nuclei with manually labeled boundaries. (b) Over-segmentation. (c) Under-segmentation. (d) Encroachment error.

The comparison of segmentation results with different methods is shown in Table II. It is observed that the LOT [5] provides only 62.03% and 67.93% of CS on our Datasets-I and II, respectively. The poor performance of the LOT technique is mainly because our testing images include a large number of nuclear clumps which cannot be efficiently split by a thresholding method. The DLM [35] only provides a slightly better performance than the LOT, with 64.72% and 68.80%



TABLE II  
COMPARISON OF NUCLEAR SEGMENTATIONS.

Datasets	Techniques	CS (%)	OS (%)	US (%)	ER (%)
Dataset-I (Ki-67)	LOT [5]	62.03	8.62	10.50	18.85
	DLM [35]	64.72	3.44	16.66	15.18
	MOW [17]	67.61	3.23	9.24	19.92
	IVW [14]	79.10	2.19	6.42	12.29
	GSM [29]	77.04	3.53	7.40	12.03
	RACM [21]	88.13	<b>1.62</b>	4.65	5.60
	Proposed	<b>90.05</b>	1.72	<b>2.88</b>	<b>5.35</b>
Dataset-II (H&E)	LOT [5]	67.93	4.76	13.59	13.73
	DLM [35]	68.80	5.66	13.39	12.15
	MOW [17]	75.49	1.40	9.24	13.87
	IVW [14]	80.81	2.38	6.44	10.36
	GSM [29]	80.95	4.90	6.58	7.56
	RACM [21]	83.89	1.96	<b>4.62</b>	9.52
	Proposed	<b>88.10</b>	<b>1.12</b>	4.90	<b>5.88</b>

of CS on our two datasets, respectively. The main reason behind this poor performance is that the DLM cannot resolve overlapping nuclei (as also mentioned in [25]), while our datasets mainly include image patches with clustered nuclei. Another reason is that the DLM requires a large number of dedicated training samples, but our training samples are limited due to the relatively small dataset. The MOW [17] provides a better performance than the LOT and DLM, which has correctly segmented 67.61% and 75.49% of cell nuclei in two datasets. The IVW [14] further improves the segmentation performance from the MOW, with around 80% of CS values on two datasets. The MOW [17] and IVW [14] perform nuclear segmentations by applying marked watershed algorithm on inner distance transform maps, both of which critically depend on the accuracy of image binarizations. In our datasets, Ki-67 stained skin images tend to be more difficult to be binarized than H&E stained skin images, and hence the performances of these two techniques [14] [17] on Ki-67 stained images are poorer than those on H&E stained images. The GSM [29] achieves a similar performance with the IVW. This technique performs watershed segmentation on a boundary probability map obtained by graph search algorithm, which is likely to under-split overlapping nuclei or over-split heterogeneous nucleus. The RACM [21] is one of the latest nuclear segmentation methods, which provides the best segmentation performance (88.13% and 83.89%) among all tested existing methods. The proposed technique achieves 90.05% and 88.10% of CS on two datasets, which are slightly better than the RACM. The RACM [21] detects nuclear seeds by a voting based algorithm, and delineates nuclear boundaries by evolving active contours. As has been verified in [30], the voting algorithm is prone to be affected by image noisy pixels which will result in false positive seeds. The active contours model for nuclear segmentation not only has a high computation complexity but also is critically dependent on the accuracy of detected nuclear seeds [19]. In comparison, the proposed technique detects nuclear seeds by a bank of multi-scale gLoG kernels, which is more accurate and efficient for blobs (i.e., nuclei) detection. The proposed mRLS based

technique delineates nuclear boundaries by analyzing multi-scale radial lines, which is more robust with different nuclear seed locations.

We also evaluate nuclear detection performances by different techniques, where the centroids of segmented nuclear regions are compared with manually labelled ground truth seeds. A nuclear centroid  $c_i$  (automatically obtained) is counted as a true positive if and only if its location is in a detection pair  $(c_i, g_j)$  for which the corresponding (nearest) ground truth seed  $g_j$  has been paired, and also their Euclidean distance is within a range of  $d$  (number of pixels) [14]. Let  $N_{CN}$  and  $N_{TP}$  denote the numbers of automatically obtained nuclear centroids and true positive detections. The performance is evaluated with respect to the recall ( $\mathcal{D}_{REC}$ ), precision ( $\mathcal{D}_{PRE}$ ) and F-measure ( $\mathcal{D}_F$ ) which are defined as follows:

$$\mathcal{D}_{REC} = \frac{N_{TP}}{N_{GT}} \times 100\% \quad (17)$$

$$\mathcal{D}_{PRE} = \frac{N_{TP}}{N_{CN}} \times 100\% \quad (18)$$

$$\mathcal{D}_F = \frac{2 \times (\mathcal{D}_{REC} \times \mathcal{D}_{PRE})}{(\mathcal{D}_{REC} + \mathcal{D}_{PRE})} \quad (19)$$

The performance of nuclear detections with different techniques are listed in Table III. Note that different  $d$  values (i.e., 6 and 4 pixels) are used for evaluation as images in Datasets-I and II have different pixel resolutions. As observed in Table III, the LOT [5] only provides 70.51% and 74.03% of F-measures on nuclear detections. The DLM [35] provides 74.16% and 76.27% of F-measures on nuclear detections. The MOW [17], IVW [14] and GSM [29] achieve intermediate performances with F-measures ranged between 77% and 86%. The RACM [21] provides 89.02% and 90.27% of F-measures, which are much better than other existing techniques. The proposed technique provides the highest F-measure values among all techniques, with 90.77% and 93.62% on Datasets-I and II, respectively. Since the centroids of segmented nuclear regions are computed and compared with manually labeled ground truth seeds for evaluating nuclear detections, the performance of nuclear detections is highly dependent on nuclear segmentations.

In order to further evaluate the accuracy of segmented nuclear contours, we compare the automatic segmentations with manual delineations by computing a boundary based metric, namely mean absolute distance (MAD) [14]. The MAD value estimates the disagreement averaged over two contours, and a better segmentation corresponds to a smaller MAD value (i.e., close to zero). However, since manual delineation of all cell nuclei is a tedious and time-consuming process, 113 and 96 nuclei are randomly chosen from Datasets-I and II, and manually delineated by using an interactive software [5]. The MAD computations are performed on these manually delineated cell nuclei. In Table III, the sixth and eleventh column separately lists the computed MAD values for different techniques. It is observed from Table III that the proposed technique has achieved the smallest MAD values (1.12 and 0.68 pixels, respectively) among all techniques, which indicates a good matching between automatically obtained nuclear boundaries and manually labeled nuclear contours.

TABLE III  
COMPARISON OF NUCLEAR DETECTIONS.

Techniques	Dataset-I ( $d = 6$ )					Dataset-II ( $d = 4$ )				
	$N_{TP}$	$\mathcal{D}_{REC}$ (%)	$\mathcal{D}_{PRE}$ (%)	$\mathcal{D}_F$ (%)	$MAD$ (px)	$N_{TP}$	$\mathcal{D}_{REC}$ (%)	$\mathcal{D}_{PRE}$ (%)	$\mathcal{D}_F$ (%)	$MAD$ (px)
LOT [5]	911	63.00	80.05	70.51	3.09	489	68.49	80.56	74.03	1.71
DLM [35]	945	65.35	86.94	74.16	2.78	497	69.61	85.10	76.27	1.53
MOW [17]	1078	74.55	79.26	76.84	1.94	567	79.41	81.35	80.37	1.15
IVW [14]	1196	82.71	80.59	81.64	1.67	640	89.64	82.69	86.02	0.88
GSM [29]	1214	83.96	76.54	80.08	1.52	634	88.80	79.65	83.97	0.87
RACM [21]	1310	90.59	87.51	89.02	1.64	654	91.60	88.98	90.27	0.92
Proposed	<b>1318</b>	<b>91.15</b>	<b>90.40</b>	<b>90.77</b>	<b>1.12</b>	<b>660</b>	<b>92.44</b>	<b>94.83</b>	<b>93.62</b>	<b>0.68</b>

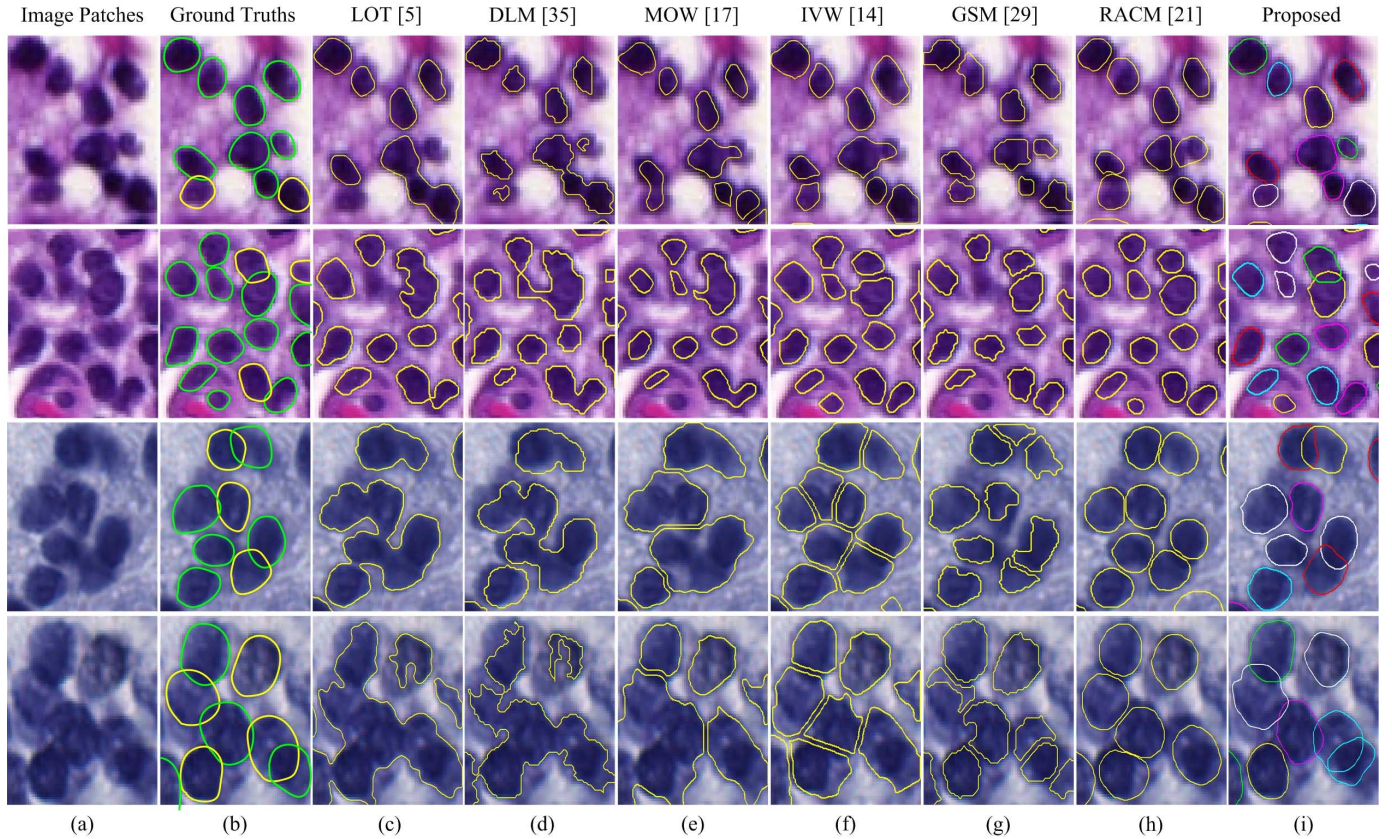


Fig. 9. Comparative nuclear segmentations. Note that column (a) shows four original image patches, while columns (b)-(i) separately show the ground truths and segmentation results obtained by different methods. In (i) nuclear boundaries obtained by the proposed technique have been indicated by different color of contours for better viewing.

### C. Qualitative Evaluations

Fig. 9 shows visual examples of nuclear segmentations by the proposed technique and several existing methods. In Fig. 9 the first two rows are H&E stained skin images, while the last two rows are Ki-67 stained skin images. The first and second columns show the original image patches and manually labeled nuclear contours, respectively. For better viewing, nuclear boundaries obtained by the proposed technique in the last column have been indicated by different color of contours (e.g., magenta, blue). As seen in Fig. 9, the LOT [5] and DLM [35] are likely to under-segment nuclear clumps. Although the MOW [17], IVW [14] and GSM [29] can segment nuclear clumps by watershed algorithms, the obtained nuclear boundaries are usually not very accurate. The RACM [21]

can provide smooth and more accurate nuclear contours, but it is limited in estimating occluded nuclear boundaries for overlapped nuclei. In comparison, the proposed technique provides a more precise and reliable segmentation results compared to existing techniques. In addition, the occluded nuclear boundaries have been generated by the proposed technique. Fig. 10 shows qualitative evaluations of the proposed technique on two large images, each of which includes hundreds of cell nuclei. Fig. 10(a) shows nuclear detection results by the gLoG kernels based method [30], where the detected seeds are indicated by (yellow) crosses. Fig. 10(b) shows the selected zoomed-in image patches of Fig. 10(a) for better viewing. Fig. 10(c) shows nuclear segmentation results by the proposed technique, and Fig. 10(d) shows selected zoomed-in image



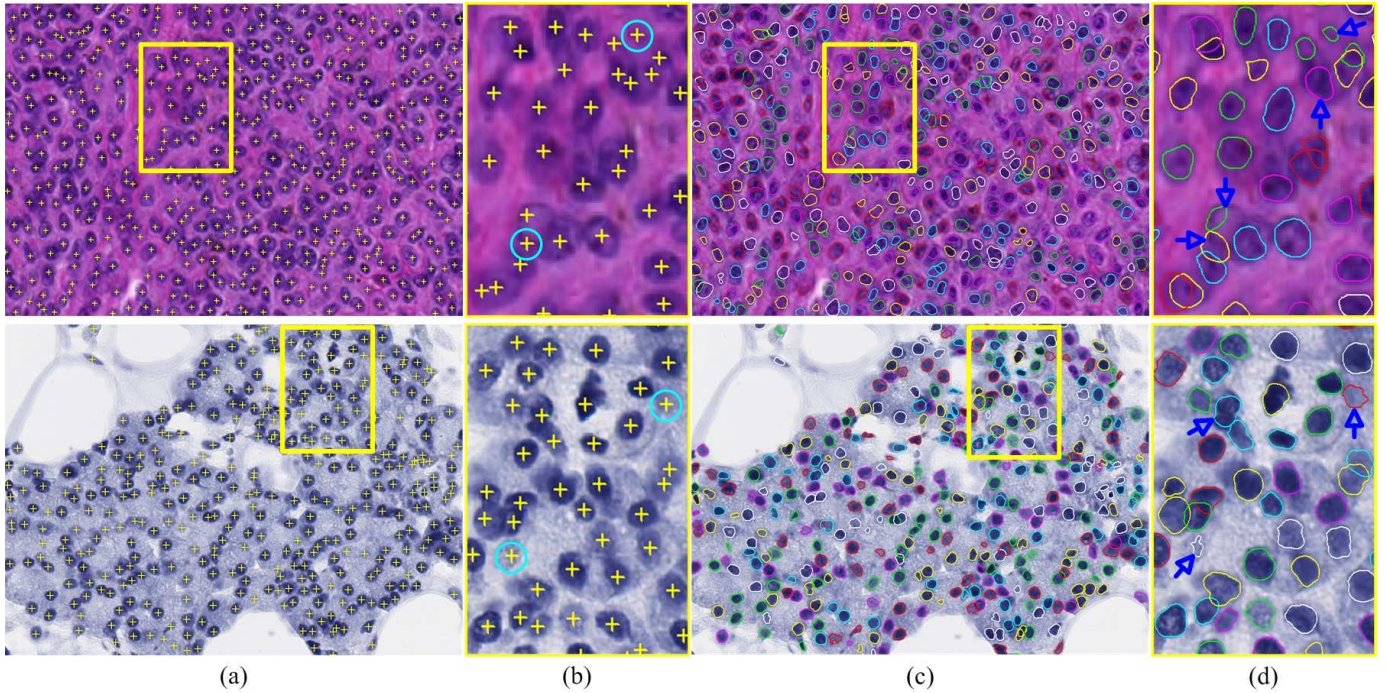


Fig. 10. Visual examples of nuclear detections and segmentations. (a) Nuclear detections. (b) Zoomed-in image patches in (a). (c) Nuclear segmentations. (d) Zoomed-in image patches in (c). Note that in (b) superimposed circles highlight false seeds detected by gLoG kernels, while in (d) superimposed arrows indicate inaccurate segmentations by the proposed technique.

patches of Fig. 10(c). Note that in Figs. 10(b)(d) superimposed circles and arrows highlight inaccurate nuclear detections and segmentations. It is observed in Fig. 10 that the proposed technique have correctly detected and segmented most of the cell nuclei in testing images, although there exist a small number of false detections and segmentations.

#### D. Sensitivity Evaluation & Computational Complexity

During the nuclear contour selection module, there are three weighting parameters ( $\lambda_1, \lambda_2, \lambda_3$ ) (see Eq.12) that should be adaptively adjusted for different applications. In this work, ( $\lambda_1, \lambda_2, \lambda_3$ ) were empirically set as (1, 1, 1) for evaluations of our two datasets. To test the sensitivities of these three parameters, we slightly vary their values and compute the correct-segmentation (CS) rates with several different combinations of ( $\lambda_1, \lambda_2, \lambda_3$ ) values. This is ( $\lambda_1, \lambda_2, \lambda_3$ )  $\in \{(1 \pm 0.5, 1, 1), (1, 1 \pm 0.5, 1), (1, 1, 1 \pm 0.5)\}$ . Fig. 11 shows the CS rates of Datasets-I and II with different combinations of weighting parameters. As observed from Fig. 11, the CS rates only vary within about 1% for both datasets when weighting parameters are slightly changed. Therefore it can be concluded that the proposed technique for nuclear segmentation is not sensitive to the marginal change of different ( $\lambda_1, \lambda_2, \lambda_3$ ) values.

In this work, all experiments were carried out on a 1.8-GHZ Intel Core i7-4500U CPU with 16-GB RAM using MATLAB 8.10. The proposed technique only takes around 30 seconds to perform nuclear detection and segmentation on a skin image like the Ki-67 stained image ( $800 \times 980$ ) shown in Fig. 10 with hundreds of cell nuclei, which indicates the efficiency of the proposed technique. The LOT [5], DLM [35], MOW [17],

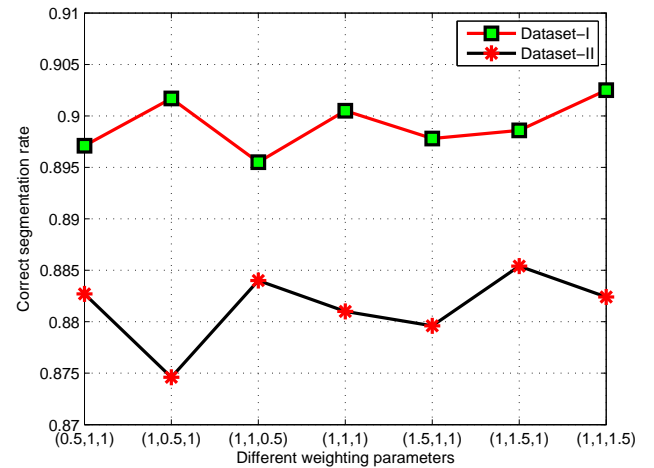


Fig. 11. Sensitivity evaluation of weighting parameters ( $\lambda_1, \lambda_2, \lambda_3$ ) on nuclear segmentation.

IVW [14], GSM [29] and RACM [21] separately take about 5s, 12s, 106s, 73s, 58s and 512s (or 8.5 minutes) to process the same image. Note that the proposed technique is well suited for parallelization, and hence parallel implementations of the algorithm (e.g., to process thousands of cell nuclei simultaneously) can be many times faster than sequential implementations.

#### IV. CONCLUSION

This paper presents an automatic technique for nuclear segmentation in skin histopathological images. The technique



relies on a bank of gLoG kernels for nuclear seeds detection, and thereafter on a mRLS with DP method for nuclear contours delineation. The proposed mRLS based technique first identifies several candidate boundary contours for each nucleus. The gradient, intensity and shape information are then integrated to determine the optimal boundary from candidate boundary contours. The Dice coefficient measure is finally applied to resolve severely overlapped nuclei. Experiments have been thoroughly performed on two datasets of skin microscopic images, which indicates that the proposed technique is superior to several existing techniques of nuclear segmentation. In addition, the proposed technique has the advantage of recognizing occluded nuclear boundaries for overlapped nuclei. Compared with level sets and active contours, the proposed technique is very efficient and suitable for parallel implementations, which can be used for processing the image with a large number of cell nuclei. In future we will analyze morphological and textural features of cell nuclei based on this work, which will help in skin cancer diagnosis.

## REFERENCES

- [1] J. Byun *et al.*, "Automated tool for the detection of cell nuclei in digital microscopic images: application to retinal images," *Molecular Vision*, vol. 12, pp. 949–960, 2006.
- [2] C. Lu *et al.*, "Automated image analysis of nuclear atypia in high-power field histopathological image," *Journal of microscopy*, vol. 258, no. 3, pp. 233–240, 2015.
- [3] M. N. Gurcan *et al.*, "Image analysis for neuroblastoma classification: Segmentation of cell nuclei," in *Proceedings of IEEE International Conference on Engineering in Medicine and Biology Society (EMBC)*, 2006, pp. 4844–4847.
- [4] S. Petushi *et al.*, "Large-scale computations on histology images reveal grade-differentiating parameters for breast cancer," *BMC medical imaging*, vol. 6, no. 1, p. 1, 2006.
- [5] C. Lu *et al.*, "A robust automatic nuclei segmentation technique for quantitative histopathological image analysis," *Analytical and Quantitative Cytology and Histology*, vol. 34, pp. 296–308, 2012.
- [6] H. Fatakdawala *et al.*, "Expectation-maximization-driven geodesic active contour with overlap resolution (emagacor): Application to lymphocyte segmentation on breast cancer histopathology," *IEEE Transactions on Biomedical Engineering*, vol. 57, no. 7, pp. 1676–1689, 2010.
- [7] H. Wang *et al.*, "Clump splitting via bottleneck detection and shape classification," *Pattern Recognition*, vol. 45, no. 7, pp. 2780–2787, 2012.
- [8] Q. Wen *et al.*, "A delaunay triangulation approach for segmenting clumps of nuclei," in *Proceedings of IEEE International Symposium on Biomedical Imaging: From Nano to Macro (ISBI)*, 2009, pp. 9–12.
- [9] O. Schmitt and S. Reetz, "On the decomposition of cell clusters," *Journal of Mathematical Imaging and Vision*, vol. 33, no. 1, pp. 85–103, 2009.
- [10] X. Bai *et al.*, "Splitting touching cells based on concave points and ellipse fitting," *Pattern recognition*, vol. 42, no. 11, pp. 2434–2446, 2009.
- [11] H. Kong *et al.*, "Partitioning histopathological images: an integrated framework for supervised color-texture segmentation and cell splitting," *IEEE Transactions on Medical Imaging*, vol. 30, no. 9, pp. 1661–1677, 2011.
- [12] L. Zhang *et al.*, "Segmentation of cytoplasm and nuclei of abnormal cells in cervical cytology using global and local graph cuts," *Computerized Medical Imaging and Graphics*, vol. 38, no. 5, pp. 369–380, 2014.
- [13] X. Qi *et al.*, "Robust segmentation of overlapping cells in histopathology specimens using parallel seed detection and repulsive level set," *IEEE Transactions on Biomedical Engineering*, vol. 59, no. 3, pp. 754–765, 2012.
- [14] H. Xu *et al.*, "An efficient technique for nuclei segmentation based on ellipse descriptor analysis and improved seed detection algorithm," *IEEE Journal of Biomedical and Health Informatics*, vol. 18, no. 5, pp. 1729–1741, 2014.
- [15] X. Yang *et al.*, "Nuclei segmentation using marker-controlled watershed, tracking using mean-shift, and kalman filter in time-lapse microscopy," *IEEE Transactions on Circuits and Systems*, vol. 53, no. 11, pp. 2405–2414, 2006.
- [16] J. Cheng and J. C. Rajapakse, "Segmentation of clustered nuclei with shape markers and marking function," *IEEE Transactions on Biomedical Engineering*, vol. 56, no. 3, pp. 741–748, 2009.
- [17] C. Jung and C. Kim, "Segmenting clustered nuclei using h-minima transform-based marker extraction and contour parameterization," *IEEE Transactions on Biomedical Engineering*, vol. 57, no. 10, pp. 2600–2604, 2010.
- [18] M. Veta *et al.*, "Automatic nuclei segmentation in H&E stained breast cancer histopathology images," *PloS one*, vol. 8, no. 7, p. e70221, 2013.
- [19] Y. Al-Kofahi *et al.*, "Improved automatic detection and segmentation of cell nuclei in histopathology images," *IEEE Transactions on Biomedical Engineering*, vol. 57, no. 4, pp. 841–852, 2010.
- [20] P. Yan *et al.*, "Automatic segmentation of high-throughput rna fluorescent cellular images," *IEEE Transactions on Information Technology in Biomedicine*, vol. 12, no. 1, pp. 109–117, 2008.
- [21] F. Xing *et al.*, "Automatic ki-67 counting using robust cell detection and online dictionary learning," *IEEE Transactions on Biomedical Engineering*, vol. 61, no. 3, pp. 859–870, 2014.
- [22] X. Zhang *et al.*, "Fine-grained histopathological image analysis via robust segmentation and large-scale retrieval," in *Proceedings of the IEEE Conference on Computer Vision and Pattern Recognition (CVPR)*, 2015, pp. 5361–5368.
- [23] M. E. Plissiti and C. Nikou, "Overlapping cell nuclei segmentation using a spatially adaptive active physical model," *IEEE Transactions on Image Processing*, vol. 21, no. 11, pp. 4568–4580, 2012.
- [24] Z. Lu *et al.*, "An improved joint optimization of multiple level set functions for the segmentation of overlapping cervical cells," *IEEE Transactions on Image Processing*, vol. 24, no. 4, pp. 1261–1272, 2015.
- [25] A. Janowczyk *et al.*, "A resolution adaptive deep hierarchical (radhical) learning scheme applied to nuclear segmentation of digital pathology images," *Computer Methods in Biomechanics and Biomedical Engineering: Imaging & Visualization*, pp. 1–7, 2016.
- [26] A. Krizhevsky *et al.*, "Imagenet classification with deep convolutional neural networks," in *Advances in neural information processing systems (NIPS)*, 2012, pp. 1097–1105.
- [27] A. Janowczyk and A. Madabhushi, "Deep learning for digital pathology image analysis: A comprehensive tutorial with selected use cases," *Journal of Pathology Informatics*, vol. 7, 2016.
- [28] K. Li *et al.*, "Optimal surface segmentation in volumetric images—a graph-theoretic approach," *IEEE transactions on pattern analysis and machine intelligence*, vol. 28, no. 1, pp. 119–134, 2006.
- [29] Y. Zhang *et al.*, "A seeding-searching-ensemble method for gland segmentation in h&e-stained images," *BMC Medical Informatics and Decision Making*, vol. 16, no. 2, p. 80, 2016.
- [30] H. Xu *et al.*, "Automatic nuclei detection based on generalized Laplacian of Gaussian filters," *accepted for publication by IEEE Journal of Biomedical and Health Informatics*, 2016.
- [31] D. Comaniciu and P. Meer, "Mean shift: A robust approach toward feature space analysis," *IEEE Transactions on Pattern Analysis and Machine Intelligence*, vol. 24, no. 5, pp. 603–619, 2002.
- [32] C. Lu *et al.*, "Detection of melanocytes in skin histopathological images using radial line scanning," *Pattern Recognition*, vol. 46, no. 2, pp. 509–518, 2013.
- [33] S. T. Acton and N. Ray, "Biomedical image analysis: tracking," *Synthesis Lectures on Image, Video, and Multimedia Processing*, vol. 2, no. 1, pp. 1–152, 2006.
- [34] A. Fitzgibbon *et al.*, "Direct least square fitting of ellipses," *IEEE Transactions on pattern analysis and machine intelligence*, vol. 21, no. 5, pp. 476–480, 1999.
- [35] K. Simonyan and A. Zisserman, "Very deep convolutional networks for large-scale image recognition," *CoRR*, vol. abs/1409.1556, 2014.
- [36] S. Ioffe and C. Szegedy, "Batch normalization: Accelerating deep network training by reducing internal covariate shift," in *Proceedings of The 32nd International Conference on Machine Learning (ICML)*, 2015, pp. 448–456.